International Journal of Nanomedicine

Dovepress
Taylor & Francis Group

Open Access Full Text Article

ORIGINAL RESEARCH

High Dihydromyricetin Loaded Biomimetic Nanoemulsion Ameliorated Early Nonalcoholic Fatty Liver Disease by Hepatic Ferroptosis Inhibition

Mingxing Yin*, Maoxian Tian*, Wenqing Wang, Chunyang Shi, Jianguo Fang, Wei Xiong

Department of Pharmacy, Tongji Hospital, Tongji Medical College, Huazhong University of Science and Technology, Wuhan, 430030, People's Republic of China

*These authors contributed equally to this work

Correspondence: Wei Xiong, Department of Pharmacy, Tongji Hospital, Tongji Medical College, Huazhong University of Science and Technology, Wuhan, 430030, People's Republic of China, Email xiongv@tjh.tjmu.edu.cn

Introduction: Nonalcoholic fatty liver disease (NAFLD) is a metabolic disorder characterized by lipid accumulation in the liver, and is often linked to ferroptosis, an iron-dependent programmed cell death driven by lipid peroxidation. Dihydromyricetin (DMY), a flavonoid from Ampelopsis grossedentata, exhibits anti-NAFLD efficiency but has low bioavailability. In this study, a high DMY-loaded biomimetic nanoemulsion (DMY-bNE) was developed using a double emulsification method with glyceryl monooleate.

Methods: DMY-bNE was characterized in vitro and in vivo including encapsulation efficiency (EE), drug-loading capacity (DLE), gastrointestinal (GI) absorption, biodistribution, pharmacokinetics, safety. High fat diet induced NAFLD mouse model was used to investigate the therapeutic effect and mechanism.

Results: DMY-bNE showed high EE (99.5%) and DLE (24.9%), promoted GI absorption, enhanced liver accumulation, improved pharmacokinetic properties and good in vivo safety. In NAFLD mice, DMY-bNE significantly ameliorated the disease progression by inhibiting hepatic ferroptosis.

Conclusion: These findings demonstrated that DMY-bNE combines enhanced drug delivery with ferroptosis inhibition, thereby offering a promising strategy for NAFLD therapy.

Keywords: dihydromyricetin, biomimetic nanoemulsion, nonalcoholic fatty liver disease, high drug loading, ferroptosis

Introduction

Nonalcoholic fatty liver disease (NAFLD) has emerged as a global health crisis characterized by excessive hepatic lipid accumulation and steatosis, with potential progression to nonalcoholic steatohepatitis (NASH), liver fibrosis, and hepatocellular carcinoma.[1,2] Driven by high-fat dietary patterns and sedentary lifestyles, NAFLD affects 29.8% of the global population and is closely associated with the obesity epidemic.[3,4] Current therapeutic strategies target hepatic lipid deposition, inflammatory responses, and fibrotic processes, including lifestyle modifications (eg, diet and exercise) and pharmacotherapeutic interventions.[5] Notably, only Resmetirom has received the Food and Drug Administration (FDA) approval for NASH treatment, underscoring the urgent need for effective therapeutics.[6,7] The pathogenesis of NAFLD involves complex interactions between lipid accumulation, oxidative stress, chronic inflammation, and programmed cell death.[8] Recently, ferroptosis was identified as a critical driver of NAFLD.[9–11] This iron-dependent form of programmed cell death is driven by lipid peroxidation, triggered by ferrous iron (Fe(II))-mediated Fenton reactions and excessive reactive oxygen species (ROS).[12,13] In the liver, Fe(II)-catalyzed lipid peroxidation exacerbates oxidative stress, disrupts glucose-lipid metabolism, and promotes hepatic steatosis. The inhibition of ferroptosis has emerged as a promising therapeutic strategy for NAFLD.[14]

The flavonoid dihydromyricetin (DMY), the major bioactive component of *Ampelopsis grossedentata* (vine tea), has demonstrated potent anti-NAFLD activity through multi-target mechanisms.[15,16] Preclinical studies have shown that DMY

https://doi.org/10.2147/IJN.S570903
Received: 16 October 2025
Accepted: 23 January 2026
Published: 4 February 2026

ameliorates NAFLD by promoting AMPK-mediated fatty acid oxidation, suppressing ROS/NF-κB-driven inflammatory signaling, improving mitochondrial function via SIRT3-dependent pathways, and inhibiting hepatic ferroptosis.[17–19] Despite its therapeutic potential, clinical translation of DMY is substantially hindered by its poor oral bioavailability (~4%). To overcome these limitations, various advanced drug delivery systems (DDS) for DMY have been developed, including liposomes, nanoparticles, nanoemulsions, phospholipid complexes, and polymeric micelles.[20–25] Nevertheless, the practical application of these existing DMY nanoformulations remains highly challenging, with encapsulation efficiency (EE) typically below 80% and drug loading efficiency (DLE) less than 10%, which is not in accordance with the guidelines of the microparticle drug delivery system of Chinese Pharmacopeia.[26] For example, DMY-loaded liposomes prepared by ethanol injection showed an EE of 41.93%,[27] while self-microemulsifying systems exhibited a DLE below 2%.[28] These limitations arise primarily from DMY's hydrophilic nature of DMY, which leads to its leakage from nanocarriers during the conventional emulsion processes.[29] Consequently, the development of novel preparation methods to significantly increase the EE and DLE of DMY-loaded nanomedicines is urgently needed.

The double emulsion method is a promising strategy for improving EE.[30] By initially encapsulating DMY within the inner aqueous phase of a W/O primary emulsion and subsequently emulsifying this W/O primary emulsion into an outer aqueous phase, DMY was effectively sequestered within the inner compartments. The intermediate oil phase acts as a barrier, minimizing the direct contact between DMY and the external water phase, thereby drastically reducing leakage and enabling a higher EE. In addition to a high loading, optimal nanocarriers require biocompatibility and targeting. Monoacylglyceride (MAG, ie glyceryl monooleate (GMO), glyceryl monostearate (GMS), glycerol monopalmitate (GMP)), with its phospholipid-mimetic amphiphilic structure, provides inherent biocompatibility.[31–33] Crucially, MAG exploits natural lipid digestion pathways; it is hydrolyzed to monoglycerides, absorbed, and incorporated into chylomicrons that undergo hepatic metabolism.[34–36] This intrinsic physiological process enables liver-targeted delivery of encapsulated drugs.

In this study, a high DMY-loaded biomimetic nanoemulsion (DMY-bNE) was prepared using a double emulsification method aimed at encapsulating high water solubility but low dissolution rate flavone in nanomedicine without leakage. DMY-bNE was designed to mimic chylomicron formation during fat absorption, in which monoolein is a natural digestion intermediate with a structure similar to that of biological membranes. DMY-bNE promoted gastrointestinal (GI) absorption, liver-targeted delivery, and fast release of DMY; inhibited hepatic ferroptosis; and in vivo ameliorated NAFLD (Scheme 1). This study integrated biomimetic drug delivery with ferroptosis-related metabolic disease therapy, which offers a novel approach to flavonoid-based nanomedicine and provides preclinical evidence for NAFLD treatment.

Experimental

Materials

(+)-DMY was prepared and purified in our laboratory (optical purity ≥ 99.5%). GMO, GMS, GMP, Hematin, sodium dithionite, triethylamine (TEA), and H_2O_2 were purchased from Macklin (China). Coumarin-6 (C6) and DiIC18 (7) (DiR) were obtained from Dalian Meilun Biotechnology Co. Ltd., China. Metformin hydrochloride (MET) was purchased from Merck, Germany. Assay kits for triglycerides (TG), total cholesterol (TC), low-density lipoprotein (LDL), high-density lipoprotein (HDL), alanine transaminase (ALT), aspartate transaminase (AST), alkaline phosphatase (ALP), urea nitrogen (BUN), lactate dehydrogenase (LDH), creatinine (CRE), malondialdehyde (MDA), nitric oxide (NO), and reduced glutathione (GSH) were supplied by the Nanjing Jiancheng Institute, China. Dihydroethidium (DHE), lipid peroxide (LPO) probe, 2,2′-azino-bis (3-ethylbenzthiazoline-6-sulfonic acid) (ABTS), and Heme assay kits were purchased from Beyotime Biotechnology (China). Isoflurane was purchased from RWD (China). Anti-Heme Oxygenase 1 (α-HO-1), anti-Nuclear factor erythroid 2-related factor 2 (α-Nrf2), anti-glutathione peroxidase 4 (α-GPX4), and α-xCT antibodies were obtained from Abcam Ltd. (Cambridge, UK). Anti-transferrin (α-TRF) and anti-lipocalin 2 (α-LCN2) antibodies were purchased from R&D Systems, Inc. (USA). Deionized ultrapure water was produced in our laboratory using a Milli-Q purification system (Merck, Germany). Analytical grade acetone and dichloromethane (DCM) were used. Methanol, phosphoric acid and formic acid (FA) were high-performance liquid chromatography (HPLC) grade. All the organic solvents were supplied by Sinopharm, China.

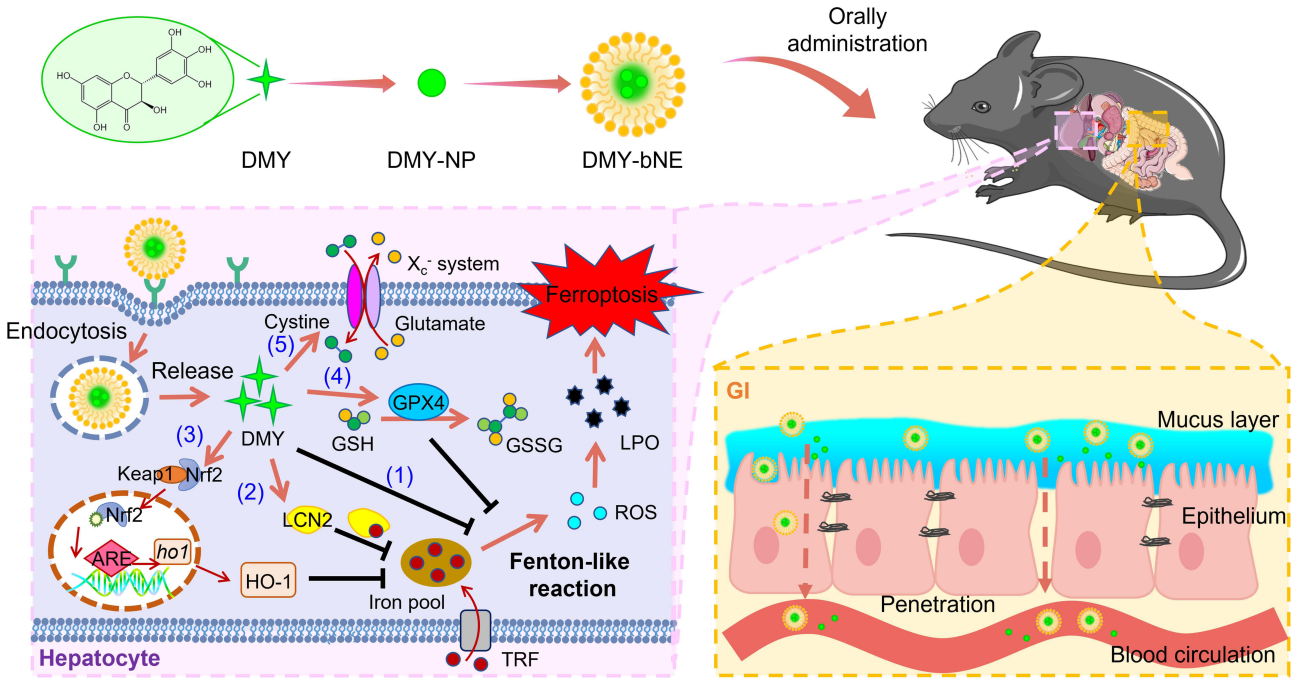

Scheme 1 Schematic illustration of the in vivo process of DMY-bNE. DMY-bNE exhibits a "core-shell" structure. Upon oral administration, DMY-bNE penetrate both mucus layer and epithelium of GI, enter blood circulation, and target to liver tissue. Following endocytosis into hepatocytes, DMY-bNE release DMY into the cytoplasm. DMY ameliorates NAFLD by inhibiting hepatic ferroptosis through multiple mechanisms: (1) directly inhibiting iron-induced Fenton-like reactions, thereby reducing the production of ROS and LPO; (2) decreasing the hepatic iron pool by up-regulating LCN2 and down-regulating TRF; (3) activating the Nrf2/HO-1 pathway to exert antioxidant effects and further reduce the hepatic iron pool; (4) up-regulating GPX4 to inhibit intracellular Fenton-like reactions; and (5) enhancing the X_c^- system to increase intracellular cystine and GSH levels.

Sprague-Dawley (SD) rats and C57BL/6J mice were obtained from the Beijing Vital River Laboratory Animal Technology Co., Ltd., China. Normal chow diet (NCD, XTI01WC) and high fat diet (HFD, XTHF60) feeds were obtained from Jiangsu Xietong Biotechnology Co. Ltd., China. All animals were maintained under specific pathogen-free (SPF) conditions at the Animal Center of Huazhong University of Science and Technology, Wuhan, China. The study was approved by the Institutional Animal Care and Use Committee of the Huazhong University of Science and Technology ([2023] IACUC Number: 3989) and conducted in compliance with the animal welfare guidelines as stipulated in the institutional guidelines (Directive 2010/63/EU) for the care and use of animals. Euthanasia or anesthesia method was in accordance with applicable veterinary guidelines (AVMA Guidelines for the Euthanasia of Animals: 2020 Edition, the American Veterinary Medical Association).

Preparation of DMY-bNE

DMY-bNE was prepared using the double emulsion method (Figure 1A). Briefly, 40 mg of (+)-DMY was dissolved in 0.3 mL of acetone to prepare DMY/acetone, while 100 mg of MAGs were dissolved in 5 mL of DCM to prepare MAG/DCM solution. Consequently, the DMY/acetone solution was dropped into the MAG/DCM solution under constant stirring of 700 rpm to prepare the primary emulsion (Figure S1A). After stirring for 5 min, the primary emulsion was added to 30 mL of water (Figure S1B). The mixture was ultrasonicated using a sonicator at 200W for 3 min (pulse 2s, room temperature) to form a secondary emulsion (Figure S1C). The secondary emulsion was stirred overnight to evaporate the organic solvent, and the resulting 30 mL of solution was DMY-bNEs. C6 loaded bNE (C6-bNE) and DiR-labeled bNE (DiR-bNE) were prepared using the same method, in which DMY was replaced with C6 and DiR, respectively.

Characterization of DMY-bNE

The particle size and zeta potential of DMY-bNEs were measured using dynamic light scattering (DLS; Zetaplus, Brookhaven, USA). Samples were diluted to ~1 mg/mL using deionized water before measurement, and all experiments repeated 5 times. The morphology was observed using transmission electron microscopy (TEM, Tecnai, Japan).

https://doi.org/10.2147/IJN.S570903

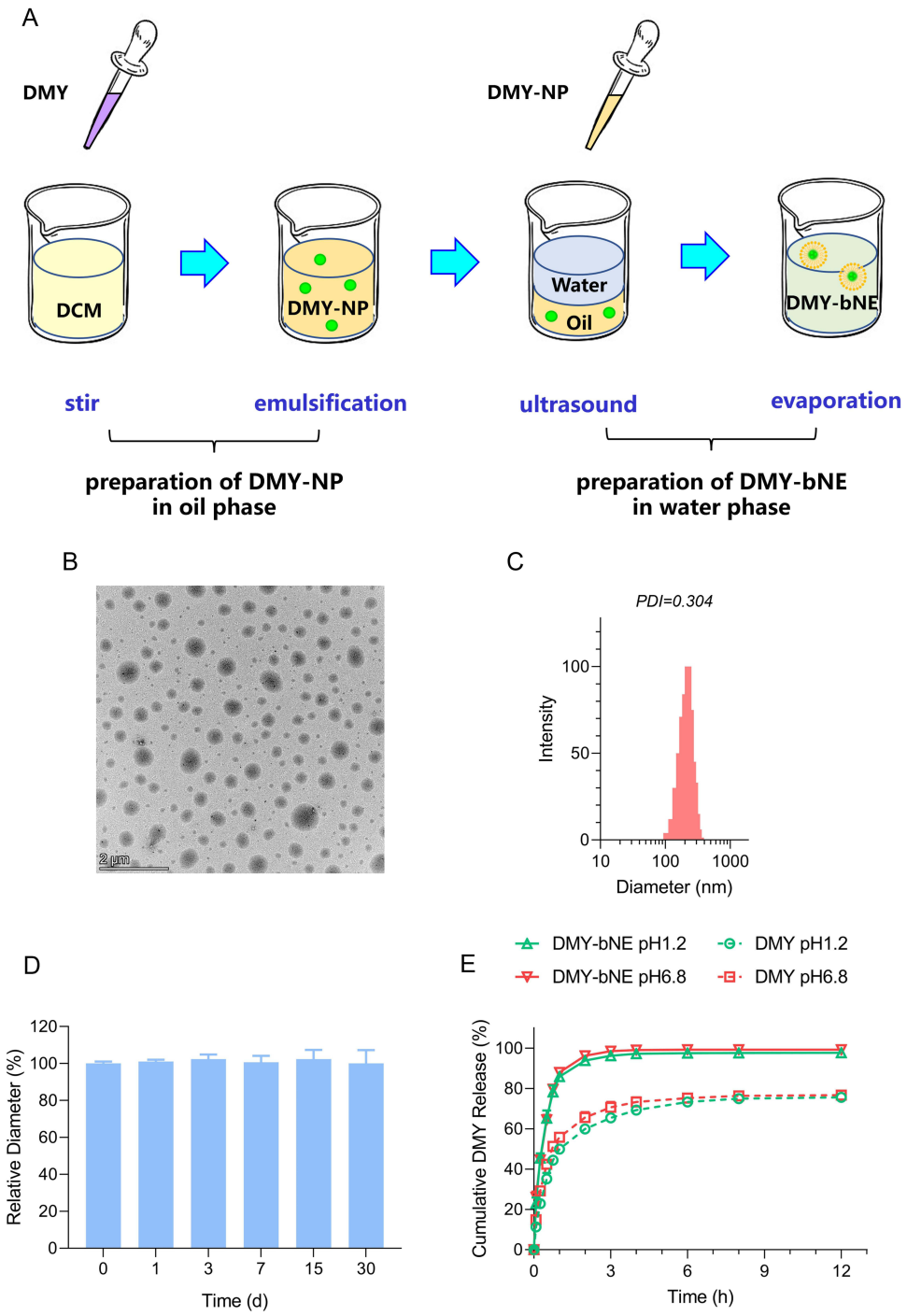

Figure 1 (**A**) Preparation process of high dihydromyricetin loaded biomimetic nanoemulsion (DMY-bNE). (**B**) Representative TEM image, (**C**) size measured by DLS, (**D**) stability and (**E**) in vitro release profiles of DMY-bNE (n =3). Scale bar represents 2 μm.

The EE of DMY-bNE was determined by HPLC (Waters e2695, USA) equipped with an ultraviolet detector and a reverse phase C_{18} column (250×4.6 mm, 5 μm). The mobile phases consisted of (A) methanol and (B) 0.1% phosphoric acid in water (v/v) at the ratio of A:B = 32:68 (v/v). The flow rate, column temperature, injection volume and detection wavelength were 1 mL/min, 30°C, 10 μL and 290 nm, respectively. The analytical method was validated for system suitability, selectivity, linearity, range, sensitivity, accuracy, precision, solution stability, and robustness according to ICH Q2 guidelines. Detail validated and results were shown in the supporting information (Figures S5 and S6, Tables S3–S7).

https://doi.org/10.2147/IJN.S570903

DMY-bNE was ultrafiltered by centrifugation (29 *g*, 2 min) and the lower phase containing unencapsulated DMY was collected. Untreated DMY-bNE and the ultrafilted lower phase were diluted with methanol and quantitatively analyzed by HPLC. The EE of DMY-bNE was calculated using the following equation.

$$EE\ (\%) = (DMY_{\ total\ fed} - DMY_{\ unencapsulated})/DMY_{\ total\ fed} \times 100.$$

The particle size of DMY-bNE was measured on predetermined days (ie 0, 1, 3, 7, 15, and 30), and the diameter changes were calculated to evaluate the storage stability of DMY-bNE.

In vitro Release

In vitro release profiles of DMY-bNE were studied under pH 1.2 and 6.8, which simulates the environment of gastric and intestinal fluids. Briefly, 1 mL of DMY-bNE and free DMY suspension were added into dialysis bags (MWCO 3500), and the bags were dialyzed in 50 mL of pH 1.2 or 6.8 release media at 37 °C with constant shaking. At predetermined time intervals (0.083, 0.25, 0.5, 0.75, 1, 2, 3, 4, 6, 8, and 12 h), 0.1mL of the release medium was collected, and the DMY concentration in the release media was determined using HPLC. The experiment repeated 3 times and the cumulative DMY release profiles were plotted.

In vivo GI Absorption

Healthy C56BL/6 mice (male, 6 w) were randomly divided into three groups (n = 9). Mice were orally administered with C6-bNE, C6 + blank bNE suspension, or free C6 suspension which were normalized using a fluorescence spectrophotometer (Hitachi F4600, Japan). At desired time intervals (0.5, 1, and 2 h), the mice were deeply anesthetized with isoflurane and then euthanized by cervical dislocation (n=3). The digestive organs (stomach and small intestine) were collected, carefully washed with cold normal saline and frozen to prepare the frozen sections. Sections were observed under a fluorescence microscope (Ti2-E; Nikon, Tokyo, Japan).

Ex vivo Imaging

To study the liver-targeting efficacy of bNE, DiR-bNE was selected as the probe. Healthy C56BL/6J mice (male, 6 w) were randomly divided into two groups (n = 12). Mice were orally treated with DiR-bNE and free DiR solution at the equivalent dose of 15 μg DiR/mouse. At predetermined time intervals (1, 4, 8, and 24 h), the mice were deeply anesthetized with isoflurane and then euthanized by cervical dislocation. Main organs (heart, liver, spleen, lung, and kidney) were collected. Ex vivo imaging of the main organs was performed using a live imaging system (Pearl Trilogy).

Pharmacokinetics

Healthy SD rats (male, BW ~250 g) were randomly divided into two groups (n = 3). After fasted food and water overnight fasting, the rats were orally administered DMY-bNE and free DMY suspension at an equivalent dose of 25 mg/kg. At predetermined time intervals (0.083, 0.25, 0.5, 0.75, 1, 2, 3, 4, 6, 8, 12, and 24 h), rats were anesthetized with isoflurane. Blood samples were collected using heparin and centrifuged to separate plasma. Plasma samples were stored at −80°C before use.

Sample solutions were prepared according to the following procedure. Briefly, the plasma samples were thawed on ice. Then, 900 μL of 0.1% FA-methanol solution was spiked into 100 μL of the plasma sample, followed by vortexing for 10 min to precipitate the protein. The mixture was then centrifugated at 10000 *g* for 10 min to separate proteins. Subsequently, 800 μL of the supernatant was collected, dried with nitrogen, and redissolved in 80 μL of 0.1% FA-methanol solution as the sample solution. The sample solutions were centrifugated at 10000 *g* for 10 min before injection into the HPLC system.

DMY concentrations at each time point were quantitatively determined, calculated, and plotted against time to construct pharmacokinetic curves. Pharmacokinetic parameters were non-compartmentally analyzed using Drug and Statistics (DAS) software (version 2.0, Mathematical Pharmacology Professional Committee, China).

In vivo Anti-NAFLD Efficacy

Healthy C57BL/6J mice (male, four weeks old) were randomly divided into two groups, ie group Healthy (n = 8) and group Model (n = 60). Mice in group Healthy were fed with NCD (11% kcal fat) as control, while mice in group Model were used to prepare NAFLD model by feeding with HFD (60% kcal fat).[37,38] After 12 weeks of HFD feeding, mice in the group Model with body weight gains > 60% (vs mice in group Healthy) were considered successful NAFLD models. The NAFLD model mice were secondly divided into five groups in random and blinding: Model, DMY, DMY + vehicle, DMY-bNE, and MET (n = 8). To simulate the clinical treatment of NAFLD patients, mice in group Model, DMY, DMY + vehicle, DMY-bNE, and MET groups were fed NCD when receiving interventions (therapy or placebo). After 3 days of adaptation, mice in group Model, DMY, DMY + vehicle, DMY-bNE, and MET groups were orally administered water (placebo, negative control), DMY suspension (25 mg/kg), DMY + blank bNE suspension (25 mg/kg), DMY-bNE (25 mg/kg), or MET (positive control, 250 mg/kg) every day for 6 weeks. Body weight was measured weekly.

At the end of the experiment, all mice were fasted overnight, deeply anesthetized with isoflurane to obtain blood samples, and euthanized by cervical dislocation to collect the liver tissues. Blood samples were centrifuged at 3000 *g* for 15 min to separate the plasma, and the levels of TG, TC, LDL, HDL, ALT, AST, and ALP were determined using the appropriate kits. Liver tissues were weighed, and the liver index was calculated using the following equation:

$$\text{Liver Index (\%)} = \text{liver weight/body weight} \times 100\%$$

Part of the liver tissue was frozen or fixed in 4% paraformaldehyde solution to prepare sections for Oil Red O (ORO) staining, hematoxylin and eosin (H&E) staining, Masson staining, DAB-enhanced Prussian blue staining, DHE fluorescent staining, LPO fluorescent staining, and immunofluorescence (HO-1, Nrf2, TRF, LCN2, GPX4, xCT) staining. The remaining liver tissue was homogenized, centrifuged, and diluted to determine the levels of GSH, H_2O_2, SOD, NO, and MDA, which were normalized to the protein content.

In vitro Heme-Catalyzed Fenton-Like Reaction

Heme, the primary storage form of ferrous iron (Fe^{2+}) in hepatocytes, exhibits biological activity by catalyzing the Fenton reaction to generate hydroxyl radicals ($HO\cdot$). Under the action of heme, H_2O_2 generates $HO\cdot$, which reacts with ABTS (colorless) to form ABTS oxidized radicals ($ABTS^{\cdot+}$) (green). The ($ABTS^{+}$) was quantitatively measured at 410 nm. To investigate the inhibitory effect of DMY on H_2O_2-derived $HO\cdot$ generation mediated by heme, ABTS reagent was used to detect $HO\cdot$. Hematin and $Na_2S_2O_3$ were completely dissolved in 1% trimethylamine in a molar ratio of 2:1 to prepare heme (0.1 mM). DMY (2 mM) was prepared in hot water. In a cuvette, ABTS solution (2.5 mM, 1 mL), DMY solution (2 mM, 1 mL), and heme solution (0.1 mM, 50 μL) were sequentially added to a cuvette. After thorough mixing, the reaction was initiated by adding a H_2O_2 solution (300 mM, 50 μL) with immediate vortexing. The optical density (O.D). (410 nm) of the solution was measured at predetermined time intervals (0, 1, 3, 5, 7.5, 10, 12.5, 15, 20, 25, and 30 min).[13] The control group was treated with an equivalent volume of purified water instead of DMY solution, and the same protocol was followed.

Safety Evaluation

The safety of DMY-bNE was evaluated in healthy C57BL/6J mice that were randomly divided into two groups (n = 6). Mice in the DMY-bNE group were orally administered 25 mg/kg DMY-bNE, whereas mice in the healthy group did not receive any intervention. All mice were fed an NCD for 6 weeks. At the end of the experiment, all mice were deeply anesthetized with isoflurane to obtain blood samples and euthanized by cervical dislocation. Main organs (the heart, liver, spleen, lung, kidney, stomach, jejunum, colon, and bone) were collected and fixed in 4% paraformaldehyde solution to prepare H&E-stained sections. Blood samples were centrifuged to separate the plasma, and the levels of ALT, AST, BUN, LDH, and CRE were determined using appropriate kits.

Statistics

Data are presented as the mean ± standard deviation (SD). Statistical analysis was performed using Student's *t*-test, One-Way ANOVA or Two-Way ANOVA with a significance level of $p < 0.05$.

Results and Discussions

Rational Design and Preparation of DMY-bNE

DMY is a dihydroflavonol with a solubility of approximately 2 mg/mL in water at 25 °C. Owing to its low dissolution rate, DMY is usually wrongly considered slight soluble in water. Encapsulating DMY in the aqueous phase is difficult because of its high thermodynamic dissolution character. Conventional emulsion preparation methods (single emulsion method, ethanol injection method, solvent evaporation method, thin-film rehydration method, etc.) cannot sequester DMY with water. DMY easily dissolves in the aqueous phase during the emulsion process, leading to the leakage and low EE (< 20% in our previous study). Herein, a double emulsion method was developed to solve this problem, which was indicated for other compounds with properties similar to those of DMY. DMY can dissolve in most organic solvents, except for halohydrocarbons, such as DCM and chloroform. Briefly, DCM was selected as the hydrophobic phase for preparation of the primary emulsion. As shown in Figure 1A, DMY was dissolved in acetone as the hydrophilic phase and the DMY/acetone solution was added dropwise to the MAG/DCM solution with constant stirring to form the primary emulsion (Figure S1A). The primary emulsion was then analyzed under a microscope, and many microcrystals approximately 2 μm in size were observed (Figure S2A). After 5 min of stabilization, the W/O primary emulsion was mixed with deionized water, followed by ultrasonication to prepare a secondary W/O/W emulsion (Figure S1B and S1C). Under a microscope, the secondary emulsion was round, with an average diameter of 10 μm (Figure S2B). The secondary emulsion was stirred overnight to evaporate organic solvent. The resultant solution was DMY-bNE, which was characterized by size/zeta potential determination, TEM imaging, EE, stability, and in vitro drug release properties. Among the three types of MAGs, GMO was found to be the best material for preparing DMY-bNE. The optimization results are presented in the Supporting Information (Table S1).

Characterization of DMY-bNE

The size and morphology of DMY-bNEs were measured using DLS and TEM, respectively. DMY-bNE had a mean hydrodynamic diameter of 190.2 ± 2.3 nm (Figure 1C) and a near-spherical shape (Figure 1B). The EE of DMY-bNE was 99.5%, which was attributed to the smart double emulsion method. During the preparation process, DMY was present in the DCM phase as micro-or nanocrystals, which prevented contact with water and led to less leakage in the aqueous phase. Compared to the single emulsion, nanoprecipitation, and solvent evaporation methods, the double emulsion method in this study greatly improved the EE of DMY, reaching almost 100%.

Diameter changes in DMY-bNE were monitored in water at 4 °C for 30 days to evaluate storage stability. As shown in Figure 1D, no significant diameter change was observed, indicating good storage stability of the formulation.

The in vitro release profiles were studied using dialysis. Media with pH 1.2 and 6.8 were used to mimic the environment of the stomach and small intestine. As shown in Figure 1E, both DMY-bNE and free DMY exhibited a rapid release during the first 3 h and reached a plateau after 8 h. The release rate and total release amount of DMY-bNE were higher than those of free DMY, indicating improved release properties of bNE and laying a good foundation for in vivo GI absorption. Furthermore, the release kinetic were fitted to First-order model (Table S2).

Stomach and Small Intestine Absorption

C6-bNE was selected as a fluorescent probe to investigate the in vivo GI absorption of bNE. C6 and the nuclei showed green and blue fluorescence, respectively. As shown in Figure 2A, C6-bNE exhibited higher green fluorescence in the gastric mucosal folds than C6 + vehicle and free C6, suggesting enhanced stomach absorption and mucosal penetration of C6-bNe.

Absorption in the small intestine exhibited similar properties. As shown in Figure 2C, higher green florescence was observed in the C6-bNE group than in the C6 + vehicle and Free C6 groups, which indicated improved small-intestine absorption of C6-bNE. Fast drug release from bNE contributed to GI absorption.

GI absorption of C6-bNE increased over time. After oral treatment with the fluorescent formulations, the green fluorescence in both the stomach and small intestine increased with time (Figure 2B and D).

https://doi.org/10.2147/IJN.S570903

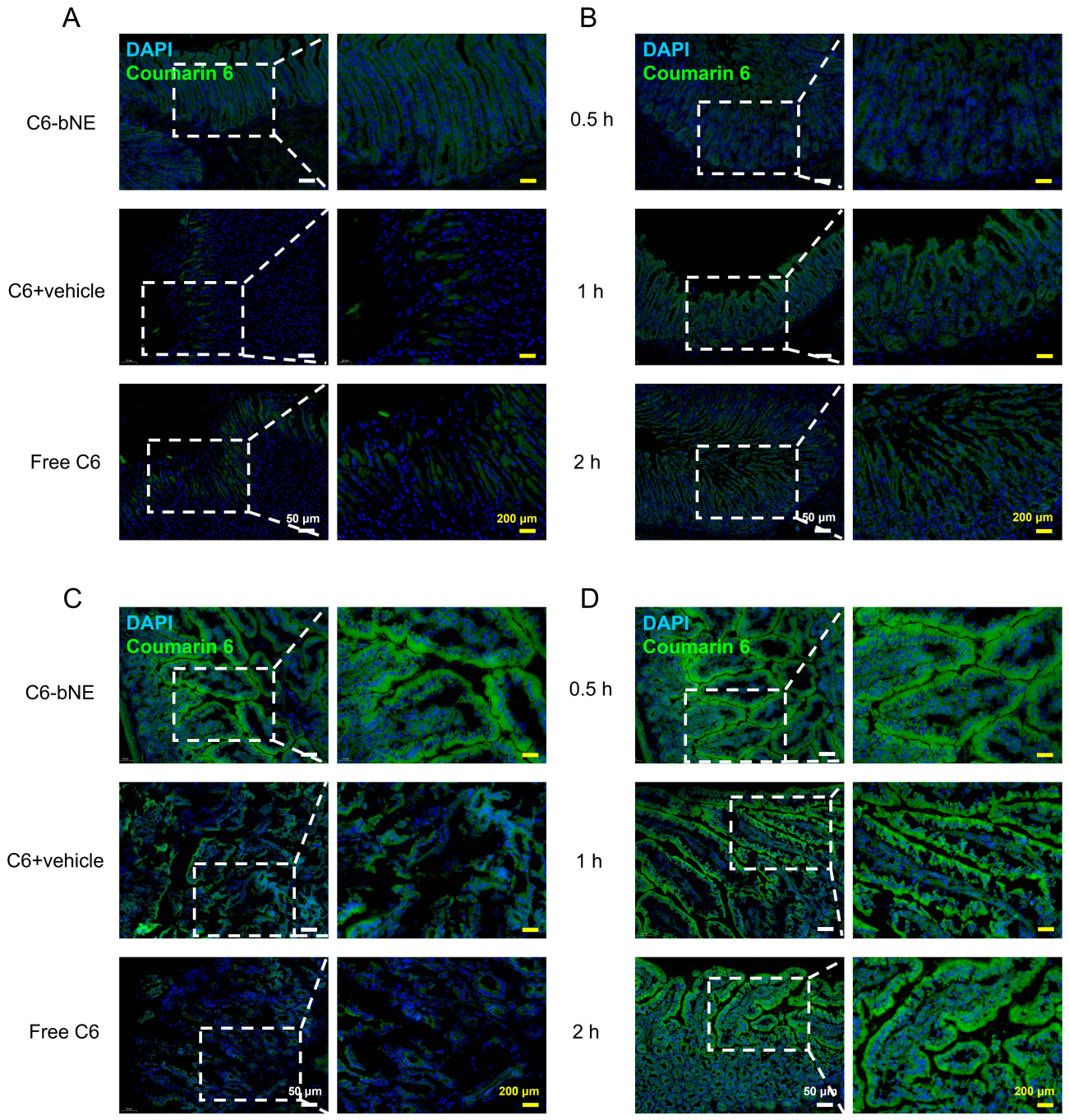

Figure 2 (**A**) Stomach and (**C**) small intestine absorption of healthy mice i.g. administrated with C6-bNE, C6 + vehicle and free C6 at 0.5 h. (**B**) Stomach and (**D**) small intestine absorption of healthy mice i.g. administrated with C6-bNE at 0.5, 1, 2 h. Representative images were displayed (n=3). Scale bars represent 50 μm (white) and 200 μm (yellow).

In vivo Liver Targeted Delivery

In vivo liver-targeted delivery was investigated using ex vivo imaging. DiR-bNE was chosen as a probe to show the drug distribution in the main organs. After oral treatment with the fluorescent formulations, the mice were sacrificed at the desired time intervals (1, 4, 8, and 24 h). The main organs of the heart, liver, spleen, lungs, and kidneys were collected and analyzed using the ISIS system. The fluorescence of DiR in liver tissue was significantly higher than that in other organs (ie heart, spleen, lung, and kidney), which indicated the successful liver-targeting efficacy of bNE (Figure 3).

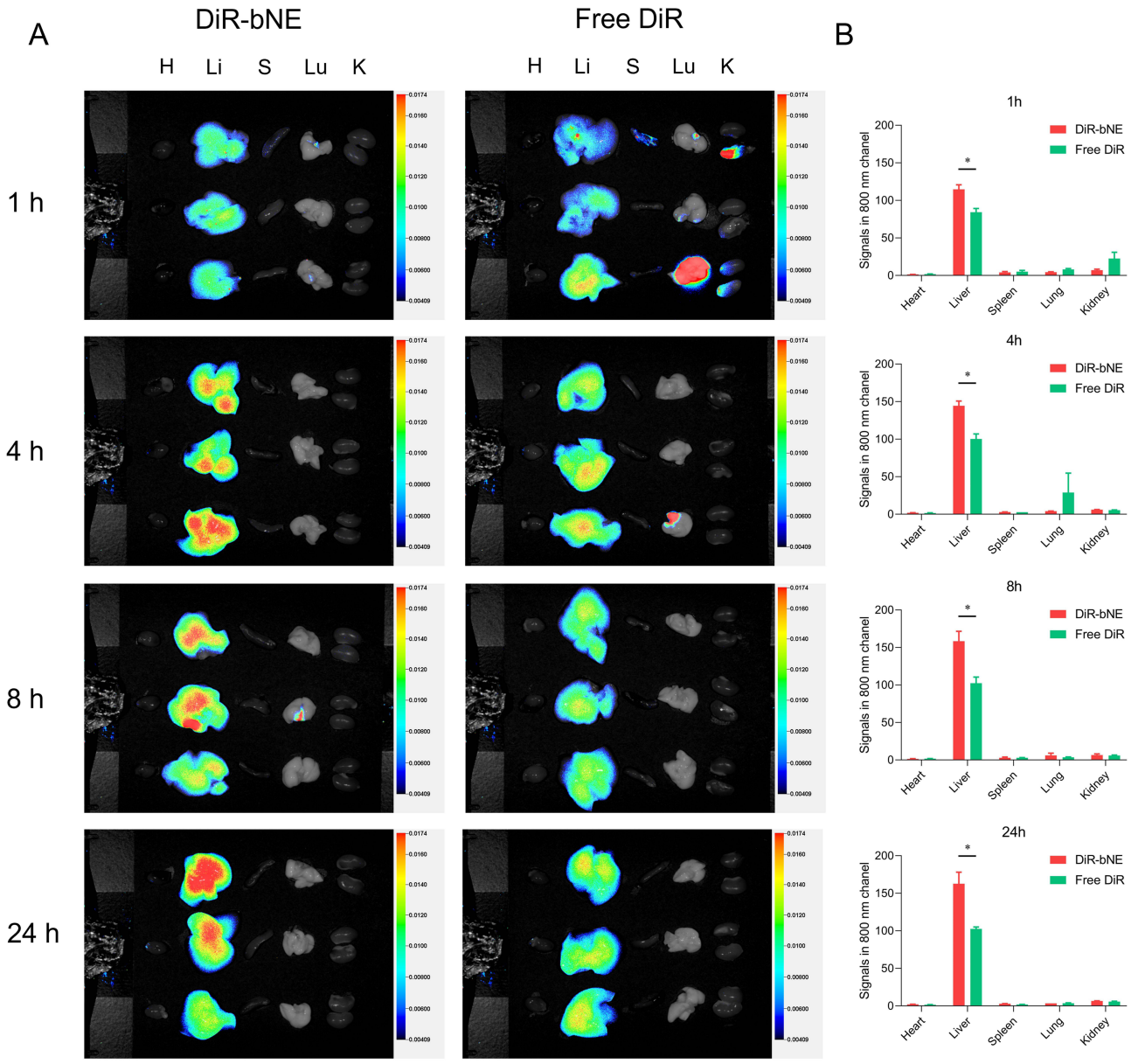

Figure 3 Biodistribution and liver targeting effect of DiR-bNE. Healthy mice were i.g. administrated with DiR-bNE and free DiR at 1, 4, 8, 24 h (n=3). (**A**) Representative ex vivo images of heart (H), liver (Li), spleen (S), lung (Lu), kidney (K) and (**B**) quantitative analysis results in different time intervals. Statistical analysis was performed using Student's *t*-test. * $p < 0.05$, vs free DiR.

Moreover, liver fluorescence signals in the DiR-bNE group were higher than those in the Free DiR group. This may be related to enhanced GI absorption via nanocarriers.

Pharmacokinetics

The pharmacokinetic profiles of DMY-bNE and free DMY were studied in healthy SD rats. As shown in Figure 4, both DMY-bNE and free DMY exhibited two stages of absorption: gastric absorption during the first 2 h, and intestinal absorption after 2 h. In the gastric absorption stage, plasma DMY concentration of DMY-bNE and free DMY reached peak at 0.25 h, and the maximum drug concentration (C_{max}) of DMY-bNE was higher than that of free DMY. Similar results were found in the intestinal absorption stage, where DMY-bNE had a higher C_{max} and reached a peak at 12 h. Pharmacokinetic parameters were calculated and are summarized in Table 1. DMY-bNE enhances in vivo blood circulation and reduces elimination. Compared with free DMY, the pharmacokinetic parameters of DMY-bNE were

https://doi.org/10.2147/IJN.S570903

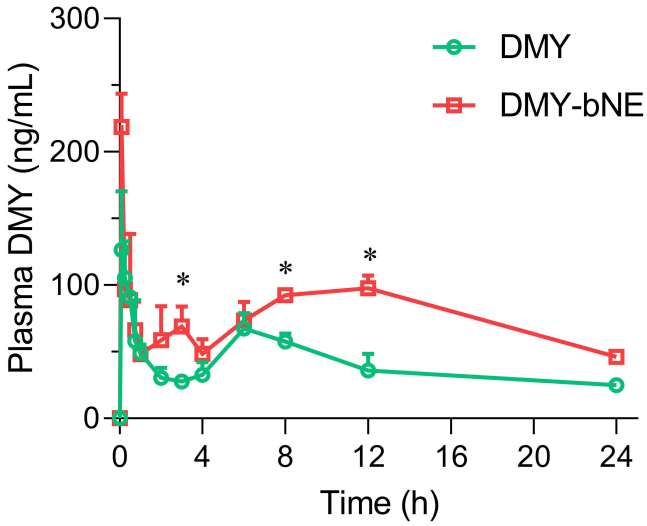

Figure 4 In vivo pharmacokinetic profiles of DMY-bNE and free DMY. Drugs were orally administrated to healthy rats at the dose of 25 mg DMY/kg, respectively (n = 3). Statistical analysis was performed using Two-Way ANOVA. * $p < 0.05$, vs DMY.

improved with 1.9 times larger area under the curve (AUC_{0-t}), 1.2 times longer half-life ($t_{1/2}$), and 60% slower clearance (CL). The prolonged presence of DMY in blood circulation might be attributed to the enhanced absorption and reduced elimination of nanosized formulations.

In vivo Anti-NAFLD Efficacy

Based on the enhanced GI absorption, increased drug accumulation in the liver, and improved bioavailability of bNE, the in vivo anti-NAFLD efficacy of DMY-bNE was further investigated in an NAFLD mouse model. The NAFLD model was established by feeding male C57BL/6J mice a HFD for 12 weeks. Obesity is an important driver in the development of NAFLD, while healthy lifestyle and weight loss are effective means of prevention and treatment of NAFLD.[1,39,40] Hence, during the 6-week drug or placebo intervention, HFD feeds were replaced by NCD feeds, and this kind of NAFLD model (ie early NAFLD) was considered self-healing and close to the clinic (Figure 5A).

Table 1 Summarized Pharmacokinetic Parameters of DMY After Orally Administration of DMY-bNE and Free DMY to Healthy Rats at the Dose of 25 mg DMY/kg, Respectively. (n = 3)

Parameters	Unit	DMY-bNE	DMY
AUC_{0-t}[a]	$\mu g \cdot L^{-1} \cdot h$	1798.81 ± 117.44[**]	955.19 ± 63.37
MRT_{0-t}[b]	h	11.00 ± 0.04[ns]	10.02 ± 0.63
$t_{1/2}$[c]	h	16.59 ± 2.87[ns]	13.74 ± 3.75
CL[d]	$L \cdot h^{-1} \cdot kg^{-1}$	5.45 ± 2.36[*]	14.08 ± 2.39
V[e]	$L \cdot kg^{-1}$	120.66 ± 33.93[**]	266.94 ± 25.12
C_{max}[f]	$\mu g \cdot L^{-1}$	218.64 ± 21.67[*]	146.79 ± 17.59
$T_{max\ 1}$[g]	h	0.25	0.25
$T_{max\ 2}$	h	12	6

Notes: [a]Area under the curve; [b]mean retention time; [c]half-life; [d]clearance; [e]apparent volume of distribution; [f]maximum drug concentration; [g]maximum drug concentration time. Statistical analysis was performed using Student's *t*-test. [*]$p < 0.05$, vs DMY; [**]$p < 0.01$, vs DMY; [ns] no significant difference, $p > 0.05$, vs DMY.

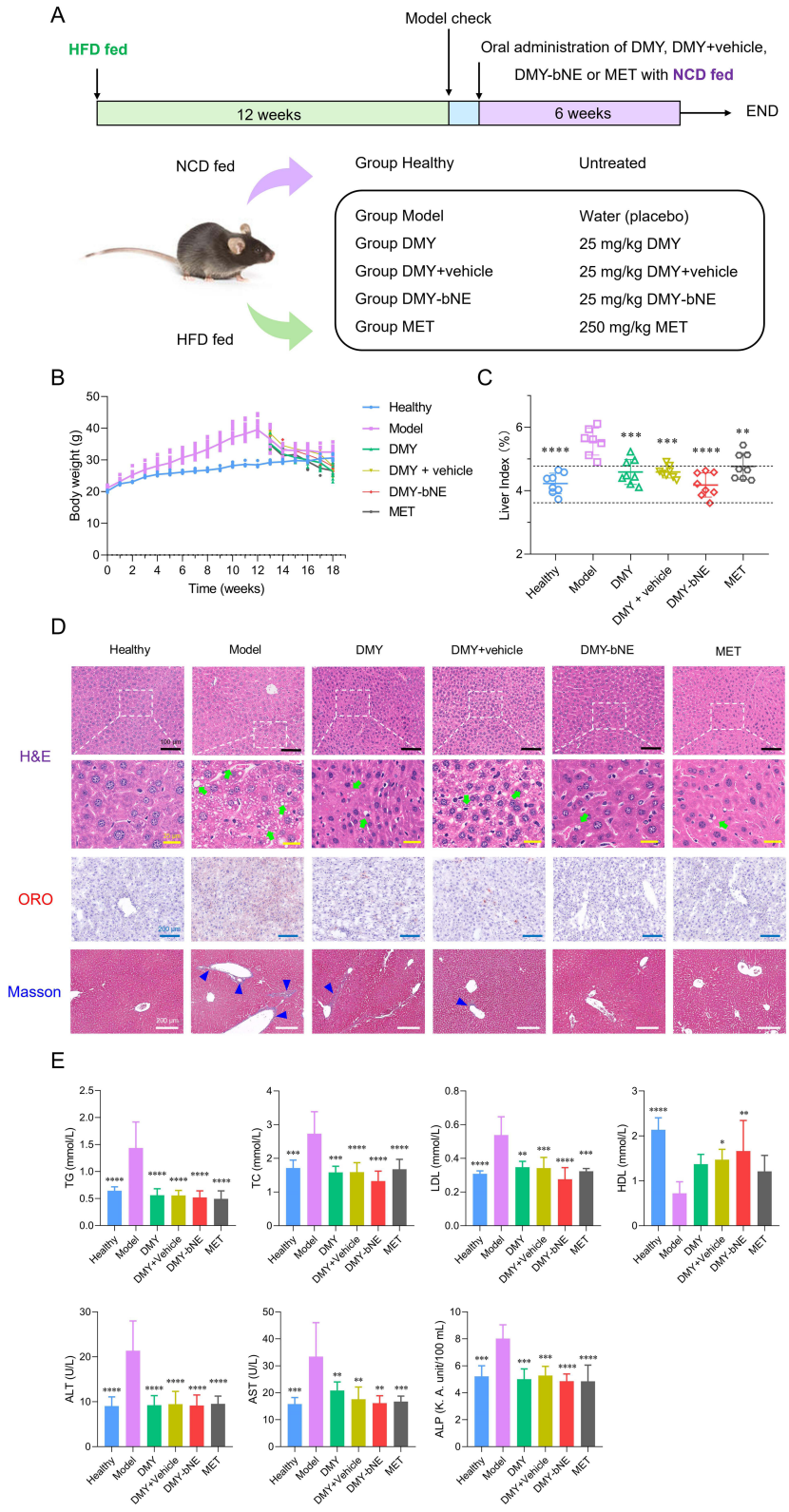

Figure 5 In vivo anti-NAFLD efficacy of DMY-bNE. Free DMY, DMY + vehicle and DMY-bNE were orally administrated to NAFLD mice at the dose of 25 mg DMY/kg, respectively, while MET was orally administrated at the dose of 250 mg MET/kg (n = 8). (**A**) Schematic illustration of the experiment, (**B**) body weight changes, (**C**) liver index, (**D**) representative HE, ORO and Masson staining, and (**E**) plasma lipid (TG, TC, LDL, HDL) and transaminase (ALT, AST, ALP) levels of healthy mice and NAFLD mice treated with water (placebo), free DMY, DMY + vehicle, DMY-bNE and MET for 6 weeks, respectively. Scale bars represent 100 μm (black), 25 μm (yellow), 200 μm (blue) and 200 μm (white). Green arrows show fatty lesions and blue triangles represent fibrosis on liver. Statistical analysis was performed using One-Way ANOVA. * $p < 0.05$, ** $p < 0.01$, *** $p < 0.001$, **** $p < 0.0001$, vs group Model.

https://doi.org/10.2147/IJN.S570903

The body weight of NAFLD model mice decreased after the feeds were changed, and mice administered DMY-bNE, DMY suspension, DMY + blank bNE suspension, and MET lost weight more significantly compared to that in the group Model (Figure 5B). Moreover, the liver index of group DMY-bNE was lower than that of group Model (Figure 5C). The decreased liver index indicated the amelioration of early NAFLD after drug intervention, which was further confirmed by H&E, ORO, and Masson staining. As shown in Figure 5D, typical steatosis was observed in H&E-staining sections of group Model, and the cytoplasmic fat vacuoles were stained red in the ORO staining sections. Compared to group Model, liver sections of group DMY-bNE, DMY + vehicle, and DMY groups exhibited fewer red-stained lipid droplets in the cytoplasm, which indicated the therapeutic effect of DMY and DMY-loaded formulations.

NAFLD induction caused dyslipidemia and hyperglycemia, with group Model showing decreased HDL and increased LDL, TG, TC and glucose levels compared group Healthy (Figures 5E and S3). Treatment with DMY-bNE reversed these lipid and glucose parameters. Importantly, mice in group DMY-bNE exhibited less fat accumulation than those in the free DMY group, which may be attributed to the structural and property advantages of DMY-bNE, such as smaller particle size, higher encapsulation efficiency, and enhanced in vitro release. Additionally, the improved liver targeting and bioavailability of DMY-bNE enable more efficient delivery of DMY to hepatocytes, directly acting on intracellular lipid metabolism processes.

Chronic HFD intake induces liver injury and fibrosis. Plasma transaminases (AST, ALT, and ALP), markers of liver injury, were markedly increased in NAFLD model mice but significantly decreased in DMY-bNE-treated mice, which implied that the intervention of DMY-bNE alleviated NAFLD related to liver injury. The severity of hepatic fibrosis is recognized as the most critical factor for predicting the prognosis of NAFLD. Masson's staining showed that the liver tissue in group Model exhibited minimal blue collagen fiber deposition, indicating mild hepatic fibrosis (Figure 5D). This mild hepatic fibrosis may be due to dietary adjustments that delay NAFLD progression. Following intervention with DMY-bNE, hepatic fibrosis was barely observed in mice, suggesting that timely early intervention in NAFLD can mitigate further deterioration.

Inhibited Hepatic Ferroptosis

The pathogenesis of NAFLD is generally attributed to chronic stimuli including lipid overload, oxidative stress, and inflammation.[41] Lipid peroxidation injury and accumulation of LPO trigger "ferroptosis" in iron-laden hepatocytes.[10,42] As the primary organ for systemic iron storage, the inhibition of hepatocyte ferroptosis represents a pivotal therapeutic target for hepatic metabolic disorders.

Building on the validated efficacy of DMY and DMY-bNE in NAFLD treatment, this study elucidated the mechanisms by which these agents suppress hepatocyte ferroptosis to reverse NAFLD pathology. Biochemical profiling of liver tissues revealed that DMY and DMY-bNE significantly decreased liver NO and MDA levels, and elevated GSH levels in NAFLD mice, while H_2O_2 and SOD levels hardly changed (Figures 6A and S4). As a central regulator of ferroptosis, GSH inhibits Heme-driven Fenton reactions via a GPX4-mediated antioxidant cascade, thereby attenuating ROS, LPO, and MDA production.[13] Prussian blue staining corroborated that DMY intervention reduced hepatic iron accumulation, consistent with the decline in Heme levels (Figure 6B–E), indicating that DMY ameliorates NAFLD by modulating redox homeostasis and iron metabolism to suppress ferroptosis.

To dissect the molecular mechanisms underlying the DMY-mediated inhibition of ferroptosis, ferroptosis-related endpoints were evaluated (Figure 6E–J). DHE fluorescence imaging demonstrated that hepatic ROS levels were markedly elevated in NAFLD mice, whereas DMY-bNE treatment reduced the number of ROS-positive foci more potently than MET treatment (Figure 6F). Concomitantly, the LPO assays showed that DMY treatment mitigated hepatic lipid peroxidation (Figure 6G). Immunofluorescence analyses revealed a dual regulatory mechanism: DMY downregulated the iron transporter TRF and upregulated the iron-sequestering protein LCN2 to reduce intracellular iron pool accumulation while restoring the Xc-/GSH/GPX4 axis function to re-establish antioxidant defense (Figure 6I and J).[43] In contrast, MET only partially modulated TRF without affecting GPX4, highlighting its ferroptosis-independent mechanism of action at the administered dosage.

Additionally, DMY enhanced the cellular antioxidant capacity by activating the Nrf2/HO-1 signaling axis. Immunofluorescence analysis confirmed the significant upregulation of Nrf2 and HO-1 expression following DMY treatment (Figure 6H). Activation of this pathway potentiates hepatic scavenging of reactive oxygen species and resistance to lipid peroxidation, thereby inhibiting ferroptosis and reversing NAFLD.[37] Collectively, DMY exerted multidimensional inhibition of hepatocyte ferroptosis by suppressing intracellular Fenton reactions, regulating iron

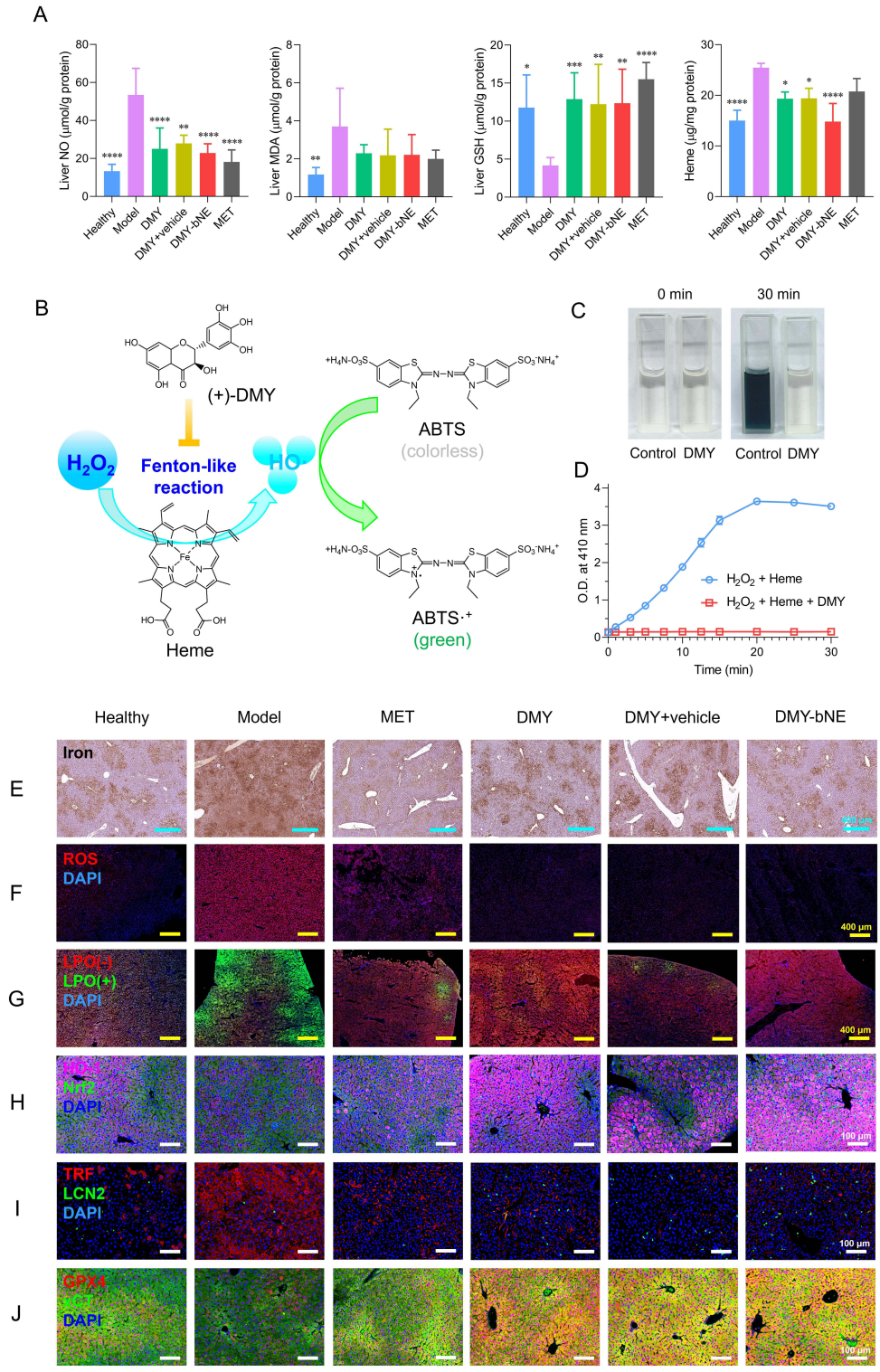

Figure 6 Mechanism of in vivo anti-NAFLD efficacy of DMY-bNE. (**A**) Liver NO, MDA, GSH and Heme levels of healthy mice and NAFLD mice treated with water (placebo), free DMY, DMY + vehicle, DMY-bNE and MET for 6 weeks, respectively (n = 8). (**B**) Schematic illustration, (**C**) pictures and (**D**) kinetic detection of in vitro inhibited Heme-catalyzed Fenton-like reaction by DMY. Representative liver (**E**) DAB enhanced Prussian blue staining, (**F**) DHE fluorescent staining, (**G**) LPO fluorescent staining, and (**H-J**) immunofluorescent staining of healthy mice and NAFLD mice treated with water (placebo), free DMY, DMY + vehicle, DMY-bNE and MET for 6 weeks, respectively. (**E**) Brown stains hepatic iron. (**F**) Red and blue fluorescence represent ROS and nucleus, respectively. (**G**) Red, green and blue fluorescence represent LPO negative area, LPO positive area and nucleus, respectively. (**H**) Pink, green and blue fluorescence represent HO-1 positive area, Nrf2 positive area and nucleus, respectively. (**I**) Red, green and blue fluorescence represent TRF positive area, LCN2 positive area and nucleus, respectively. (**J**) Red, green and blue fluorescence represent GPX4 positive area, xCT positive area and nucleus, respectively. Scale bars represent 400 μm (cyan), 400 μm (yellow) and 100 μm (white). Statistical analysis was performed using One-Way ANOVA. * $p < 0.05$, ** $p < 0.01$, *** $p < 0.001$, **** $p < 0.0001$, vs group Model.

https://doi.org/10.2147/IJN.S570903

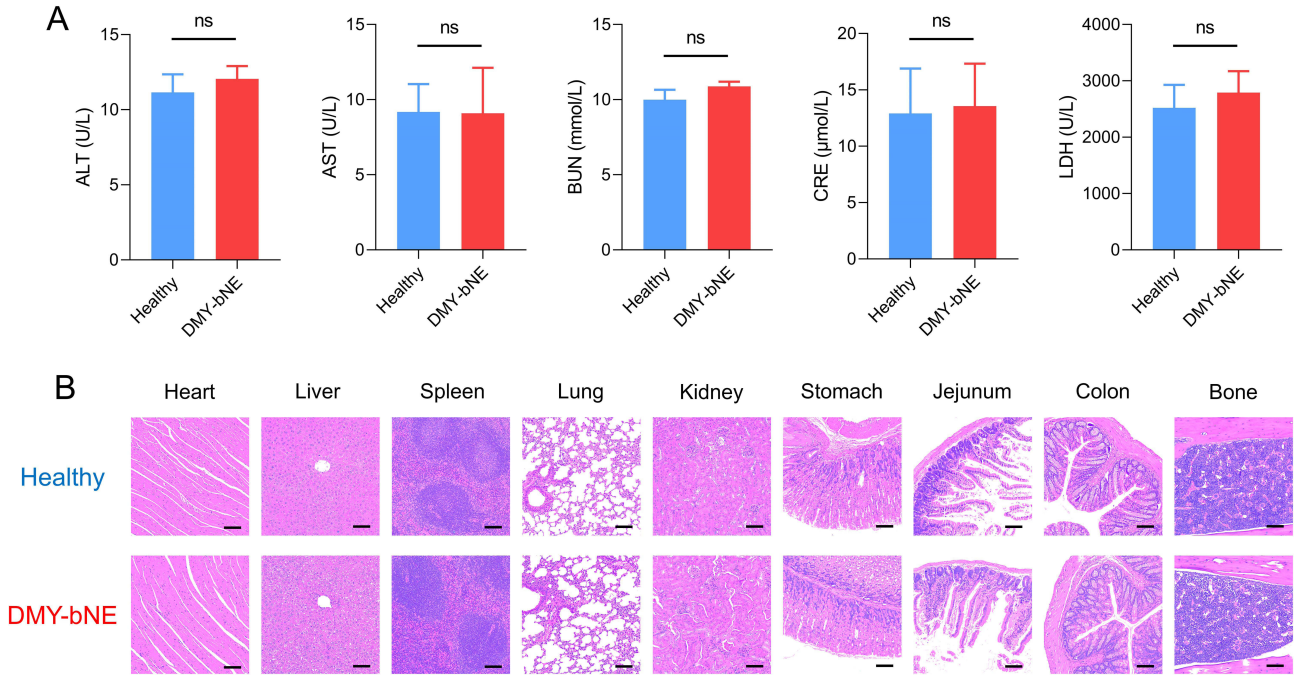

Figure 7 In vivo safety evaluation of DMY-bNE. (**A**) Plasma ALT, AST, BUN, CRE, LDH levels and (**B**) representative HE staining of main organs (heart, liver, spleen, lung, kidney, stomach, jejunum, colon and bone) of healthy mice treated with water and DMY-bNE for 6 weeks, respectively (n = 6). Scale bars represent 100 μm (black). Statistical analysis was performed using Student's *t*-test. ns, no significant difference.

metabolism proteins, reducing LPO accumulation, and engaging Nrf2-dependent antioxidant responses, providing novel mechanistic insights into its therapeutic efficacy against NAFLD.

After oral administration and GI absorption, DMY-bNE can be targeted to hepatocytes and endocytosed, subsequently releasing DMY. DMY ameliorated NAFLD by inhibiting intracellular ferroptosis via the following mechanisms (Scheme 1): (1) direct inhibition of iron-induced Fenton-like reactions, thereby reducing the production of ROS and LPO; (2) decreasing the hepatic iron pool by upregulating LCN2 and downregulating TRF; (3) activating the Nrf2/HO-1 pathway to exert antioxidant effects and further reducing the hepatic iron pool; (4) upregulating GPX4 to inhibit intracellular Fenton-like reactions; and (5) enhancing the Xc- system to increase intracellular cystine and GSH levels.

Safety Evaluation

In vivo safety of DMY-bNE was evaluated using healthy C57BL/6J mice. After oral administration of DMY-bNE (25 mg/kg, qd) for six weeks, all mice survived without abnormal behavior. Plasma ALT, AST, BUN, CRE, and LDH levels in mice treated with DMY-bNE were within the normal range and were not significantly different from those in healthy mice (Figure 7A). Moreover, H&E staining of the main organs (heart, liver, spleen, lung, kidney, stomach, jejunum, colon, and bone) showed no pathological changes (Figure 7B), demonstrating the safety of orally administered DMY-bNE via oral administration.

Conclusion

In summary, we successfully developed a DMY-loaded biomimetic nanoemulsion using a double emulsification method. This rationally designed system significantly enhances GI absorption, reduces systemic clearance, and improves oral bioavailability of DMY. DMY-bNE achieved targeted liver delivery and effectively ameliorated NAFLD progression by inhibiting hepatocyte ferroptosis. Prospectively, all the ingredients in the preparation process are safe and FDA approved, which makes it feasible for industrial fabrication of DMY-bNE. This functionally advanced nanoplatform demonstrates

favorable biosafety, therapeutic efficacy and industrialization prospects, establishing a novel strategy for NAFLD intervention and providing a translatable paradigm for natural product delivery.

Data Sharing Statement

Data are available from the corresponding author on reasonable request.

Ethics Approval

The study was approved by the Institutional Animal Care and Use Committee of the Huazhong University of Science and Technology ([2023] IACUC Number: 3989) and conducted in compliance with the animal welfare guidelines as stipulated in the institutional guidelines (Directive 2010/63/EU) for the care and use of animals. Euthanasia or anesthesia method was in accordance with applicable veterinary guidelines (AVMA Guidelines for the Euthanasia of Animals: 2020 Edition, the American Veterinary Medical Association).

Acknowledgment

The authors thank the Analytical and Testing Center of HUST for FTEM measurements.

Funding

This work was supported by the National Natural Science Foundation of China (82404585), Key Research and Development Program of Hubei Province of China (2023BCB063, 2023BCB130, 2024AFB1010, 2024BCB034 and 2024BCB037) and Project of Administration of Traditional Chinese Medicine of Hubei Province of China (ZY2025L241).

Disclosure

The authors report no conflicts of interest in this work.

References

1. Rinella ME, Neuschwander-Tetri BA, Siddiqui MS, et al. AASLD practice guidance on the clinical assessment and management of nonalcoholic fatty liver disease. *Hepatology*. 2023;77:1797–1835. doi:10.1097/HEP.0000000000000323
2. Kanwal F, Neuschwander-Tetri BA, Loomba R, Rinella ME. Metabolic dysfunction-associated steatotic liver disease: update and impact of new nomenclature on the American Association for the Study of Liver Diseases practice guidance on nonalcoholic fatty liver disease. *Hepatology*. 2024;79:1212–1219. doi:10.1097/HEP.0000000000000670
3. Younossi ZM, Golabi P, Paik JM, Henry A, Van Dongen C, Henry L. The global epidemiology of nonalcoholic fatty liver disease (NAFLD) and nonalcoholic steatohepatitis (NASH): a systematic review. *Hepatology*. 2023;77:1335–1347. doi:10.1097/HEP.0000000000000004
4. Miao L, Targher G, Byrne CD, Cao YY, Zheng MH. Current status and future trends of the global burden of MASLD. *Trends Endocrinol Metab*. 2024;35:697–707. doi:10.1016/j.tem.2024.02.007
5. Younossi ZM, Zelber-Sagi S, Henry L, Gerber LH. Lifestyle interventions in nonalcoholic fatty liver disease. *Nat Rev Gastroenterol Hepatol*. 2023;20:708–722. doi:10.1038/s41575-023-00800-4
6. Keam SJ. Resmetirom: first Approval. *Drugs*. 2024;84:729–735. doi:10.1007/s40265-024-02045-0
7. Petta S, Targher G, Romeo S, et al. The first MASH drug therapy on the horizon: current perspectives of resmetirom. *Liver Int*. 2024;44:1526–1536. doi:10.1111/liv.15930
8. Allameh A, Niayesh-Mehr R, Aliarab A, Sebastiani G, Pantopoulos K. Oxidative stress in liver pathophysiology and disease. *Antioxidants*. 2023;12:1653. doi:10.3390/antiox12091653
9. Qi J, Kim JW, Zhou ZX, Lim CW, Kim B. Ferroptosis affects the progression of nonalcoholic steatohepatitis via the modulation of lipid peroxidation-mediated cell death in mice. *Am J Pathol*. 2020;190:68–81. doi:10.1016/j.ajpath.2019.09.011
10. Wu J, Wang Y, Jiang RT, et al. Ferroptosis in liver disease: new insights into disease mechanisms. *Cell Death Discovery*. 2021;7. doi:10.1038/s41420-021-00660-4
11. Zhang T, Wang MY, Wang GD, et al. Metformin improves nonalcoholic fatty liver disease in db/db mice by inhibiting ferroptosis. *Eur J Pharmacol*. 2024;966:176341. doi:10.1016/j.ejphar.2024.176341
12. Tsurusaki S, Tsuchiya Y, Koumura T, et al. Hepatic ferroptosis plays an important role as the trigger for initiating inflammation in nonalcoholic steatohepatitis. *Cell Death Dis*. 2019;10. doi:10.1038/s41419-019-1678-y
13. Zhao M, Jin ZK, Xia C, et al. Inhibition of free heme-catalyzed Fenton-like reaction prevents non-alcoholic fatty liver disease by hepatocyte-targeted hydrogen delivery. *Biomaterials*. 2023;301:122230. doi:10.1016/j.biomaterials.2023.122230
14. Cai WS, Wu S, Ming XP, et al. IL6 derived from macrophages under intermittent hypoxia exacerbates NAFLD by promoting ferroptosis via MARCH3-led ubiquitylation of GPX4. *Adv Sci*. 2024;11. doi:10.1002/advs.202402241
15. Wang C, Xiong W, Perumalla SR, Fang J, Sun CC. Solid-state characterization of optically pure (+)Dihydromyricetin extracted from *Ampelopsis grossedentata* leaves. *Int J Pharm*. 2016;511:245–252. doi:10.1016/j.ijpharm.2016.07.018

16. Li Z, Ali I, Qiu J, et al. Eco-friendly and facile synthesis of antioxidant, antibacterial and anticancer dihydromyricetin-mediated silver nanoparticles. *Int J Nanomed*. 2021;16:481–492. doi:10.2147/IJN.S283677
17. Gong H, Xu HM, Li MY, Zhang DK. Molecular mechanism and therapeutic significance of dihydromyricetin in nonalcoholic fatty liver disease. *Eur J Pharmacol*. 2022;935:175325. doi:10.1016/j.ejphar.2022.175325
18. Yang Y, Qiu W, Xiao JY, Sun J, Ren X, Jiang LX. Dihydromyricetin ameliorates hepatic steatosis and insulin resistance via AMPK/PGC-1α and PPARα-mediated autophagy pathway. *J Transl Med*. 2024;22:309. doi:10.1186/s12967-024-05060-7
19. Zeng XL, Yang JN, Hu O, et al. Dihydromyricetin ameliorates nonalcoholic fatty liver disease by improving mitochondrial respiratory capacity and redox homeostasis through modulation of SIRT3 signaling. *Antioxid Redox Signaling*. 2019;30:163–183. doi:10.1089/ars.2017.7172
20. Hou GQ, Xu CF, Cheng KX, et al. Metabolic mechanisms of Dihydromyricetin and strategies for enhancing its bioavailability: a recent review. *Food Chem*. 2025;485:144470. doi:10.1016/j.foodchem.2025.144470
21. Wang CG, Tong Q, Hou XL, Hu SY, Fang JG, Sun CC. Enhancing bioavailability of dihydromyricetin through inhibiting precipitation of soluble cocrystals by a crystallization inhibitor. *Cryst Growth Des*. 2016;16:5030–5039. doi:10.1021/acs.cgd.6b00591
22. Zhao XY, Shi CY, Zhou XY, et al. Preparation of a nanoscale dihydromyricetin-phospholipid complex to improve the bioavailability: in vitro and in vivo evaluations. *Eur J Pharm Sci*. 2019;138:104994. doi:10.1016/j.ejps.2019.104994
23. Yan QH, Li MQ, Dong LY, et al. Preparation, characterization and protective effect of chitosan-Tripolyphosphate encapsulated dihydromyricetin nanoparticles on acute kidney injury caused by cisplatin. *Int J Biol Macromol*. 2023;245:125569. doi:10.1016/j.ijbiomac.2023.125569
24. Ye J, Bao S, Zhao SY, et al. Self-assembled micelles improve the oral bioavailability of dihydromyricetin and anti-acute alcoholism activity. *AAPS Pharm Sci Tech*. 2021;22. doi:10.1208/s12249-021-01983-2
25. Zhang YT, Wang HQ, Xu CL, et al. Rubicon siRNA-encapsulated liver-targeting nanoliposome is a promising therapeutic for non-alcoholic fatty liver disease. *Int J Pharm*. 2025;672:125291. doi:10.1016/j.ijpharm.2025.125291
26. C.P. commission, chinese pharmacopoeia (2025 Edition), volume IV, China Medical Science Press2025.
27. Luo F, Zeng DD, Chen RX, et al. PEGylated dihydromyricetin-loaded nanoliposomes coated with tea saponin inhibit bacterial oxidative respiration and energy metabolism. *Food Funct*. 2021;12:9007–9017. doi:10.1039/D1FO01943K
28. Dong JX, Wang S, Mao JM, et al. Preparation of dihydromyricetin-loaded self-emulsifying drug delivery system and its anti-alcoholism effect. *Pharmaceutics*. 2023;15(9):2296. doi:10.3390/pharmaceutics15092296
29. Mirchandani Y, Patravale VB, Brijesh S. Solid lipid nanoparticles for hydrophilic drugs. *J Control Release*. 2021;335:457–464. doi:10.1016/j.jconrel.2021.05.032
30. Ding SK, Serra CA, Vandamme TF, Yu W, Anton N. Double emulsions prepared by two-step emulsification: history, state-of-the-art and perspective. *J Control Release*. 2019;295:31–49. doi:10.1016/j.jconrel.2018.12.037
31. Desai HH, Serajuddin AM. Development of lipid-based SEDDS using digestion products of long-chain triglyceride for high drug solubility: formulation and dispersion testing. *Int J Pharm*. 2024;654:123953. doi:10.1016/j.ijpharm.2024.123953
32. Nguyen TH, Hanley T, Porter CJH, Boyd BJ. Nanostructured liquid crystalline particles provide long duration sustained-release effect for a poorly water soluble drug after oral administration. *J Control Release*. 2011;153:180–186. doi:10.1016/j.jconrel.2011.03.033
33. Li J, Yin M, Tian M, Fang J, Xu H. Stiff-soft hybrid biomimetic nano-emulsion for targeted liver delivery and treatment of early nonalcoholic fatty liver disease. *Pharmaceutics*. 2024;16:1303. doi:10.3390/pharmaceutics16101303
34. Attia MF, Anton N, Chiper M, et al. Biodistribution of X-ray iodinated contrast agent in nano-emulsions is controlled by the chemical nature of the oily core. *Acs Nano*. 2014;8:10537–10550. doi:10.1021/nn503973z
35. Huang SZ, Yin HH, Tian F, et al. Effects of mono-and di-glycerides/phospholipids (MDG/PL) on the bioavailability of lutein and DHA in rats: more effective for lutein. *Food Bioscience*. 2025;69:106815. doi:10.1016/j.fbio.2025.106815
36. Prajapati HN, Dalrymple DM, Serajuddin ATM. A comparative evaluation of mono-, di- and triglyceride of medium chain fatty acids by lipid/surfactant/water phase diagram, solubility determination and dispersion testing for application in pharmaceutical dosage form development. *Pharm Res*. 2012;29:285–305. doi:10.1007/s11095-011-0541-3
37. Lei S, Wu Q, Zhang B, Lu MQ, Xia Y, Li N. Liver-targeting nanoparticles GA-MSe@AR treat NAFLD through dual lipid-lowering and antioxidant efficacy. *Int J Nanomed*. 2025;20:5017–5037. doi:10.2147/IJN.S510577
38. Huang XF, Yang J, Hu YY, et al. Protective effects of galnac-modified red blood cell-derived extracellular vesicles against liver diseases. *Int J Nanomed*. 2025;20:8993–9017. doi:10.2147/IJN.S510937
39. Iannone V, Babu AF, Lok J, et al. Changes in liver metabolic pathways demonstrate efficacy of the combined dietary and microbial therapeutic intervention in MASLD mouse model. *Mol Metabol*. 2023;78:101823. doi:10.1016/j.molmet.2023.101823
40. Fang CL, Liu SJ, Yang WQ, et al. Exercise ameliorates lipid droplet metabolism disorder by the PLIN2-LIPA axis-mediated lipophagy in mouse model of non-alcoholic fatty liver disease. *Biochimica Et Biophysica Acta*. 2024;1870:167045. doi:10.1016/j.bbadis.2024.167045
41. Stefan N, Cusi K. A global view of the interplay between non-alcoholic fatty liver disease and diabetes. *Lancet Diabetes Endocrinol*. 2022;10:284–296. doi:10.1016/S2213-8587(22)00003-1
42. Gautheron J, Gores GJ, Rodrigues CMP. Lytic cell death in metabolic liver disease. *J Hepatol*. 2020;73:394–408. doi:10.1016/j.jhep.2020.04.001
43. Hou T, Tang Y, Wang L, Peng L, Ci X. Dihydromyricetin alleviates lipid peroxidation-induced Pyroptosis by inhibiting xCT ubiquitination and degradation in experimental COPD model. *Phytomedicine*. 2025;144:156929. doi:10.1016/j.phymed.2025.156929